Journal of
Materials Chemistry A

ROYAL SOCIETY
OF CHEMISTRY

PAPER

View Article Online
View Journal

Check for updates

Cite this: DOI: 10.1039/d6ta01727d

Rational design of B-site single-atom doped $LaMnO_3$ for CO chemical looping combustion: a DFT study

Zhongze Bai[a] and Kai H. Luo *[ab]

Received 27th February 2026
Accepted 3rd May 2026

DOI: 10.1039/d6ta01727d

rsc.li/materials-a

Perovskite oxides such as $LaMnO_3$ are widely investigated as oxygen carriers (OCs) in chemical looping combustion (CLC) due to their tunable catalytic and structural properties. In this study, density functional theory (DFT) calculations were employed to explore the effects of B-site single-atom doping on the CO oxidation performance of $LaMnO_3$. Among 25 possible doped configurations, eight were identified as thermodynamically stable, providing a basis for further activity analysis. The adsorption and activation of CO on these stable doped surfaces were examined at the electronic level, followed by evaluation of the reaction energy barriers. Five doped structures (V-, Cr-, Ni-, Rh-, and Cd-$LaMnO_3$) displayed lower barriers than pristine $LaMnO_3$, with Ni-$LaMnO_3$ showing the lowest value of 0.770 eV, corresponding to a 61% reduction. *Ab initio* molecular dynamics (AIMD) simulations further confirmed the kinetic stability of these low-barrier structures under CLC conditions. Finally, structure–activity–stability relationships were explored, revealing that the +3 ionic radius and the Bader charge transfer of the doped atom serve as robust descriptors for predicting both stability and catalytic activity. Collectively, these findings provide atomic-level insights for the rational design of doped perovskite oxides with enhanced performance in CO CLC, demonstrating the potential of targeted B-site doping strategies to improve catalytic activity.

1 Introduction

In recent years, with ongoing industrialization, the extensive use of fossil fuels has led to a significant increase in atmospheric CO_2 concentrations, exacerbating global warming and climate change.[1–3] Given that combustion is a major pathway for fossil fuel utilization, considerable research efforts have been devoted to developing carbon-capture-enabled combustion technologies to mitigate CO_2 emissions. These strategies include pre-combustion capture, post-combustion capture, and oxy-fuel combustion, all of which remain under active investigation.[4] Among these technologies, chemical looping combustion (CLC) has emerged as a novel and cost-effective CO_2 capture approach, as CO_2 capture is an inherent feature of the combustion process.[5,6] A typical CLC system consists of a fuel reactor (FR), an air reactor (AR), and oxygen carrier (OC) particles that circulate between the two reactors.[7] In the FR, fuel is oxidized by lattice oxygen from the OC, which is then regenerated in the AR. As the fuel and air never come into direct contact, the fuel reactor exhaust contains only CO_2 and H_2O, enabling straightforward separation *via* condensation.

The development of high-performance OCs is one of the key challenges in CLC technology. Initially, monometallic oxides were extensively investigated as OCs due to their high reactivity; however, they often fail to meet the stringent mechanical and chemical stability requirements of CLC processes.[8] Consequently, composite metal oxides formed through physical mixing or chemical integration of two or more metal oxides have been proposed to enhance the mechanical and chemical stability of oxygen carriers.[9,10] Among them, perovskite oxides are particularly attractive due to their excellent redox activity and outstanding thermal stability, and their general chemical formula is commonly expressed as ABO_3.[11]

$LaMnO_3$, a representative manganese-based perovskite oxide, has attracted a lot of attention as the OC for CLC owing to its high stability and reactivity. For example, a series of studies have investigated the performance of $LaMnO_3$ OCs in CLC processes involving CH_4,[12–14] CO,[15] and Hg^0 pollutant removal,[16,17] through both experimental and density functional theory (DFT) studies. Nevertheless, the reaction energy barriers of $LaMnO_3$ remain relatively high compared with those of monometallic oxides such as CuO, resulting in lower reaction rates and reduced overall efficiency.[18,19] Therefore, enhancing the reactivity of $LaMnO_3$ remains essential. The catalytic activity of perovskite oxides is closely associated with the reducibility of the B-site transition metal, and can be effectively improved by

---

[a] *Department of Mechanical Engineering, University College London, Torrington Place, London WC1E 7JE, UK*

[b] *Center for Combustion Energy, Department of Energy and Power Engineering, Key Laboratory for Thermal Science and Power Engineering of Ministry of Education, Low Carbon Energy and CCUS Research Center, Institute for Carbon Neutrality, Tsinghua University, Beijing, 10084, China. E-mail: k.luo@ucl.ac.uk*

doping different metal cations into the B-site lattice.[20] In addition, recent studies have shown that the catalytic performance of perovskite oxides can be effectively understood and predicted using electronic structure descriptors, such as charge-transfer energy, band orbital characteristics, and oxygen p-band centre, derived from experimental and DFT analyses.[21–24] These descriptors provide fundamental insights into catalytic activity trends and offer a powerful framework for establishing structure–activity relationships and guiding rational catalyst design.[25–29]

As a key intermediate formed during solid fuel conversion and incomplete combustion, CO plays a pivotal role in governing the reaction pathways, combustion efficiency, and overall performance of chemical looping combustion systems. Recently, significant efforts have been devoted to enhancing CO oxidation over perovskite oxides through B-site metal doping. For instance, Singh and co-workers reported that low-level Pd(II)-doped $BaCeO_3$ perovskites exhibited high low-temperature CO oxidation activity, attributed to cationic Pd(II) promoting lattice and surface oxygen activation.[30] Farhang and co-workers demonstrated that substituting 10% of Cu with Pd in $LaSrCuO_4$ perovskites prepared *via* a low-temperature solid-state method could improve catalytic performance for CO oxidation and methane combustion.[31] Subsequently, they extended this work by synthesizing $LaSrCuO_4$ perovskites with both Pd and Pt substitutions, showing that B-site doping enhances catalytic activity through increased lattice oxygen mobility, larger surface area, and H_2-spillover effects.[32] Yuan and co-workers synthesized a series of nanostructured $SiTiO_3$ perovskites with B-site partial substitution (Co, Fe, Mn, Ni, Cu) *via* one-step flame spray pyrolysis, demonstrating that Co-doped $SrTiO_3$ exhibits superior CO oxidation and CH_4 dehydrogenation performance due to enhanced oxygen vacancies, reducibility, and water resistance.[33] Experiments, DFT calculations, and microkinetic modelling were carried out by Yang and co-workers to investigate CO catalytic combustion over Ni-doped $LaCoO_3$ perovskites, showing that Ni doping enhances low-temperature activity by promoting lattice oxygen reactivity, with the Co–O–Co and Co–O–Ni sites serving as main active centres and the reaction following a Mars–van Krevelen mechanism.[34] The above studies successfully demonstrated that the catalytic activity of perovskite oxides for CO oxidation can be enhanced through B-site metal doping. However, they largely overlooked the investigation of B-site metal doping in the highly attractive $LaMnO_3$ OCs, particularly regarding their CO oxidation performance in CLC.

DFT calculations have been widely employed to elucidate surface reaction mechanisms and establish structure–activity relationships in heterogeneous catalysis at the atomic level.[35–38] Accordingly, DFT calculations were employed in this work to investigate the performance of 25 potential transition metal dopants (Sc, Ti, V, Cr, Mn, Fe, Co, Ni, Cu, Zn, Mo, Tc, Ru, Rh, Pd, Ag, Cd, Hf, Ta, W, Re, Os, Ir, Pt, and Au) substituting a single Mn atom in $LaMnO_3$ during CO oxidation. We first examined the stability of the doped structures. For the stable configurations, we then evaluated the adsorption behaviour of CO on their surfaces, followed by the adsorption of CO_2 produced from the reaction between CO and lattice oxygen. Subsequently, the reaction energy barriers and transition-state structures for CO oxidation, including CO_2 formation and desorption, were systematically analysed. Finally, we examined descriptors derived from the intrinsic properties of the active sites to assess structural stability and catalytic activity, thereby establishing the structure–activity–stability relationships for doped $LaMnO_3$.

2 Methods

2.1 Catalyst models

The $LaMnO_3$ bulk structure adopted in this work crystallizes in an orthorhombic lattice with the *Pnma* space group, obtained from the Materials Project database (MP-17554).[39] A Mn-terminated $LaMnO_3$ (010) surface was selected for modelling, as this surface has been reported to exhibit favourable energetic stability and catalytic activity.[40,41] A p(2 × 2) slab model comprising eight atomic layers was employed, separated by a 20 Å vacuum region to prevent interactions between adjacent periodic images. During geometry optimization, the lower four layers were constrained, whereas the upper four layers were allowed to relax to improve computational efficiency. As shown in Fig. 1, after geometry optimization, the $LaMnO_3$ (010) surface exposes six potential active sites, namely Mn, O_1, O_2, $bridge_1$, $bridge_2$, and a surface vacancy. Single-atom B-site doping was modelled by substituting one surface Mn atom with a dopant atom. A total of 25 transition metal elements were considered as possible dopants: Sc, Ti, V, Cr, Mn, Fe, Co, Ni, Cu, Zn, Mo, Tc, Ru, Rh, Pd, Ag, Cd, Hf, Ta, W, Re, Os, Ir, Pt, and Au.

2.2 DFT calculations

All first-principles calculations were carried out using the Vienna *Ab initio* Simulation Package (VASP) within the generalized gradient approximation (GGA), employing the Perdew–Burke–Ernzerhof (PBE) exchange–correlation functional.[42–44] The interaction between core and valence electrons was described using the projector augmented-wave method, with a plane-wave kinetic energy cutoff set to 500 eV. Structural optimizations were considered converged when the total energy change was below 1.0×10^{-5} eV and the residual atomic forces were less than 0.03 eV $Å^{-1}$. Brillouin zone integrations were performed using Monkhorst–Pack *k*-point meshes of 5 × 4 × 5 for the bulk unit cell and 2 × 2 × 1 for the surface supercell models. Transition states and activation energies were determined using the climbing-image nudged elastic band (CI-NEB) approach.[45] Unless otherwise specified, all CI-NEB calculations were performed using the same computational parameters as those employed in the static calculations. Transition states were further validated through vibrational frequency analysis. Post-processing and workflow management were conducted using the VASPKIT[46] and QVASP[47] packages, while structural models were visualized with the VESTA[48] program. The bonding characteristics were analysed *via* crystal orbital Hamilton population (COHP) calculations employing the Local Orbital Basis Suite Towards Electronic-Structure Reconstruction (LOBSTER).[49] Adsorption and activation energies were corrected

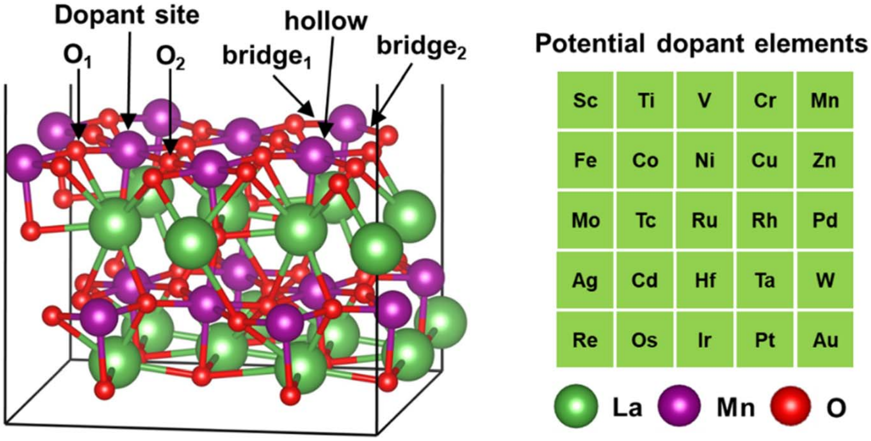

Fig. 1 Schematic illustration of the $LaMnO_3$ (010) surface with the corresponding potential dopant elements.

for zero-point energy (ZPE) using vibrational frequency calculations.

Although $LaMnO_3$ is often considered a correlated oxide, the choice of the Hubbard U parameter in PBE+U calculations remains ambiguous and varies widely in the literature, potentially introducing additional uncertainty.[50] Previous studies have demonstrated that GGA-derived effective Bader charges for La-based perovskites agree well with GGA+U results, indicating negligible self-interaction errors for the 3d electrons.[51] Moreover, the PBE functional has been shown to reliably reproduce key reaction energies and activation barriers for $LaMnO_3$-based CLC materials in good agreement with experiments.[15,41] Therefore, to ensure consistency with prior studies and to enable efficient large-scale calculations, the present work employed the standard PBE functional without an explicit +U correction.

The formation energy (E_f) is used as a thermodynamic stability criterion for doped surfaces and is calculated according to the following equation:

$$E_f = E_{\text{M-LaMnO}_3\text{-Slab}} - E_{\text{LaMnO}_3\text{-Slab}} - E_{\text{M-refer}} + E_{\text{Mn-refer}} \quad (1)$$

where, $E_{\text{M-LaMnO}_3\text{-Slab}}$ and $E_{\text{LaMnO}_3\text{-Slab}}$ represent DFT-calculated total energies of the doped and pristine $LaMnO_3$ slabs, respectively. $E_{\text{Mn-refer}}$ and $E_{\text{M-refer}}$ correspond to the reference energies of Mn and the dopant element M, respectively. And Mn and M referenced to its stable phase under CLC conditions (800–1000 K), as summarized in Table S1. To account for the energy of the missing or excess oxygen atoms (E_O), the correction $[E(H_2O) - E(H_2)]$ was employed instead of $0.5E(O_2)$, mitigating the well-known overbinding error of GGA functionals in describing the O_2 molecule. This correction strategy follows the approach reported in ref. 52.

Ab initio molecular dynamics (AIMD) simulations were carried out in the NVT ensemble with a Nosé–Hoover thermostat for 10 ps using a time step of 0.5 fs to assess the kinetic stability of the doped structures.

The adsorption energy (E_{ads}), reaction energy barrier (E_b), and overall reaction energy (E_{all}) were calculated according to eqn (2)–(4), respectively.

$$E_{\text{ads}} = E(\text{AB}) - E(\text{A}) - E(\text{B}) \quad (2)$$

$$E_b = E(\text{TS}) - E(\text{IS}) \quad (3)$$

$$E_{\text{all}} = E(\text{FS}) - E(\text{IS}) \quad (4)$$

where, E_{AB}, E_{A}, E_{B}, E_{TS}, E_{IS}, and E_{FS} denote the energies of the adsorption complex, substrate, adsorbate, transition state, initial state, and final state, respectively.

3 Results and discussion

3.1 Structure and stability of catalysts

Thermodynamic stability represents the first criterion in constructing metal-doped M-$LaMnO_3$ systems. In this work, the formation energy (E_f) was employed to evaluate the thermodynamic stability of the doped structures. It is worth noting that for the reference pristine system (undoped $LaMnO_3$), the formation energy is strictly 0 eV, which serves as a reasonable benchmark for dopant screening. In general, a favourable dopant incorporation is indicated by a negative formation energy ($E_f < 0$). Considering the typical uncertainty of DFT calculations (approximately 0.2 eV), doped structures with formation energies below 0.2 eV were considered sufficiently stable for further analysis, following the criterion adopted in ref. 52. Fig. 2 presents the E_f of metal-doped $LaMnO_3$ (010) surfaces. Among the 25 possible doped structures considered, 8 configurations exhibit thermodynamic stability according to the formation energy criterion, namely Ti-$LaMnO_3$, V-$LaMnO_3$, Cr-$LaMnO_3$, pristine $LaMnO_3$, Ni-$LaMnO_3$, Mo-$LaMnO_3$, Rh-$LaMnO_3$, and Cd-$LaMnO_3$. The optimized structures of these stable configurations are shown in Fig. S1.

For the doped $LaMnO_3$ systems that were identified as stable, the local metal–oxygen bond lengths were analysed to elucidate the structural effects induced by different dopants. As shown in Fig. 3, the M–O_1 bond lengths are generally shorter than the corresponding M–O_2 bonds, and both exhibit the same trends across different dopant elements. In this work, we primarily focus on the M–O_1 bond lengths as representative of

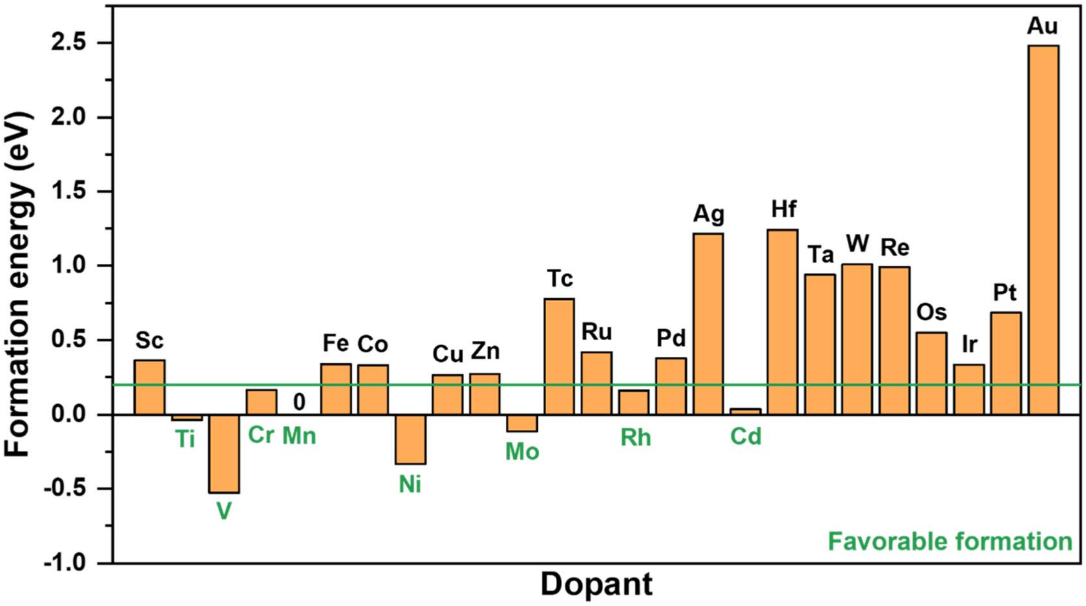

Fig. 2 Formation energy (E_f) for metal doped $LaMnO_3$ (010).

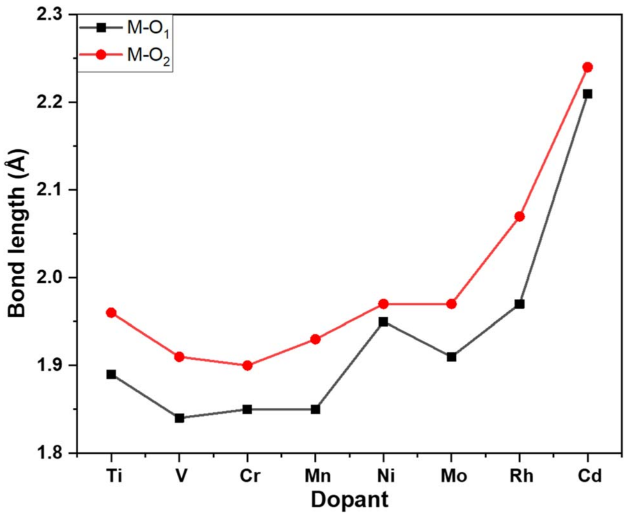

Fig. 3 Bond lengths between dopant metal and oxygen atoms (M–O_1 and M–O_2 correspond to O_1 and O_2 sites, respectively).

the local metal–oxygen coordination. The average M–O_1 bond lengths span a range from 1.84 to 2.21 Å, indicating a pronounced dopant-dependent modification of the local coordination environment. Specifically, Ti-, V-, Cr-, and Mn-doped $LaMnO_3$ exhibit relatively short M–O_1 bond lengths (1.84–1.89 Å), suggesting strong metal–oxygen interactions that are favourable for maintaining structural integrity. In contrast, Ni-, Mo-, and Rh-doped systems show moderately elongated M–O bonds (1.91–1.97 Å), reflecting a weakened yet stable metal–oxygen bonding environment. Notably, the Cd-doped $LaMnO_3$ displays the longest M–O_1 bond length (2.21 Å). These results demonstrate that even among dynamically stable doped structures, the M–O bond lengths vary substantially with dopant identity, highlighting the ability of metal substitution to tune the local lattice structure of $LaMnO_3$.

3.2 Adsorption and activation of CO on doped $LaMnO_3$ surface

The adsorption and activation of CO on catalyst surfaces are the first step in CO catalytic oxidation. We considered three adsorption configurations (C-side, O-side, and CO-side) on eight thermodynamically stable catalyst surfaces, evaluating six distinct adsorption sites on each surface. After geometry optimizations, the most stable adsorption structures are shown in Fig. 4. In all cases, CO adsorption preferentially occurs through the C-end at the dopant metal sites. The CO adsorption energies range from −0.277 eV to −1.629 eV, with the strongest adsorption observed on the Cd-$LaMnO_3$ surface and the weakest on pristine $LaMnO_3$. For all investigated surfaces, significant charge transfer occurs during CO adsorption, predominantly from the metal atoms to the CO molecule, with transferred charges ranging from 0.05 *e* to 0.29 *e*. The largest charge transfer is found on the Mo-$LaMnO_3$ surface, while the smallest occurs on Cd-$LaMnO_3$. The pronounced charge transfer and relatively strong adsorption energies across all surfaces indicate that CO adsorption proceeds *via* chemisorption rather than weak physisorption. The M–C bond lengths fall within the range of 1.755–2.390 Å, with the longest bond observed on Cd-$LaMnO_3$ and the shortest on pristine $LaMnO_3$. Moreover, elongation of the C–O bond is observed for CO adsorbed on all surfaces, with bond lengths ranging from 1.148 Å to 1.171 Å. These values are significantly larger than the gas-phase C–O bond length of 1.128 Å,[53] indicating effective activation of the CO molecule upon adsorption.

It should be noted that both the preferred adsorption site and the adsorption energy of CO on the $LaMnO_3$ surface

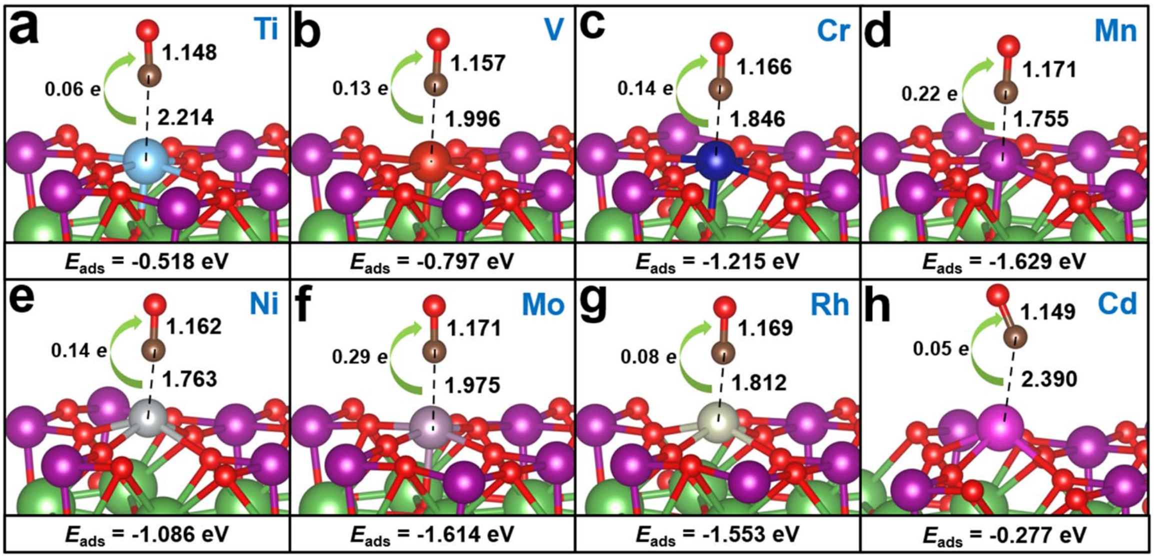

Fig. 4 Adsorption configurations of CO on (a) Ti-$LaMnO_3$, (b) V-$LaMnO_3$, (c) Cr-$LaMnO_3$, (d) pristine $LaMnO_3$, (e) Ni-$LaMnO_3$, (f) Mo-$LaMnO_3$, (g) Rh-$LaMnO_3$, and (h) Cd-$LaMnO_3$ surfaces. The unit for bond length is Å. Atom colours: Mn (purple), La (green), O (red), and C (brown).

obtained in this work differ from some previous study.[15] These discrepancies are mainly due to differences in computational software and parameters. For example, previous studies may have employed CASTEP with ultrasoft pseudopotentials and lower plane-wave cutoff energies, whereas the present work uses VASP with PAW potentials and a higher cutoff, along with stricter convergence criteria. Importantly, all adsorption and reaction calculations in this work were performed using a consistent computational framework, ensuring reliable trend comparisons.

The correlation analysis is used to reveal the intrinsic relationships among key CO adsorption features. The Pearson correlation coefficients among the adsorption energy, M–C bond length, C–O bond length, and CO charge transfer are summarized in Fig. 5. It should be noted that only parameters with absolute correlation coefficients exceeding 0.8 ($|r| > 0.8$) are regarded as strongly correlated and are therefore emphasized. A strong negative correlation ($r = -0.983$, $p < 0.001$) is observed between the adsorption energy and the C–O bond length, indicating that stronger CO adsorption is accompanied by a more pronounced elongation of the C–O bond. This suggests that CO activation is closely coupled with adsorption strength. In contrast, the adsorption energy shows a positive correlation with the M–C bond length ($r = 0.834$, $p < 0.01$), implying that stronger adsorption corresponds to a shorter M–C bond. Furthermore, the M–C bond length exhibits a clear negative correlation with the C–O bond length ($r = -0.833$, $p < 0.01$), indicating that a shorter and stronger metal–carbon bond is accompanied by a more pronounced elongation of the C–O bond. The analysis indicates a strong interrelationship among the adsorption energy, M–C bond length, and C–O bond length, where stronger adsorption corresponds to a shorter M–C bond and a longer C–O bond.

To gain deeper insight into the interaction between the dopant atom and CO, partial density of states (PDOS) and crystal orbital Hamilton population (COHP) analyses were performed, as shown in Fig. S2 and S3, respectively, with an energy window from −8 eV to 4 eV relative to the Fermi level. Taking Mo-$LaMnO_3$ as a representative example to illustrate the electronic interactions, the antibonding π^* orbitals of gas-phase CO are located above the Fermi level (Fig. 6a). Upon adsorption, these π^* orbitals strongly hybridize with the Mo-derived states near the Fermi level (Fig. 6c). The downward shift and partial occupation of the CO π^* states account for the effective adsorption of CO on the Mo-$LaMnO_3$ surface. Moreover, a larger fraction of the CO antibonding states moves below the Fermi level and becomes populated by electrons transferred from the transition-metal surface, leading to the activation and

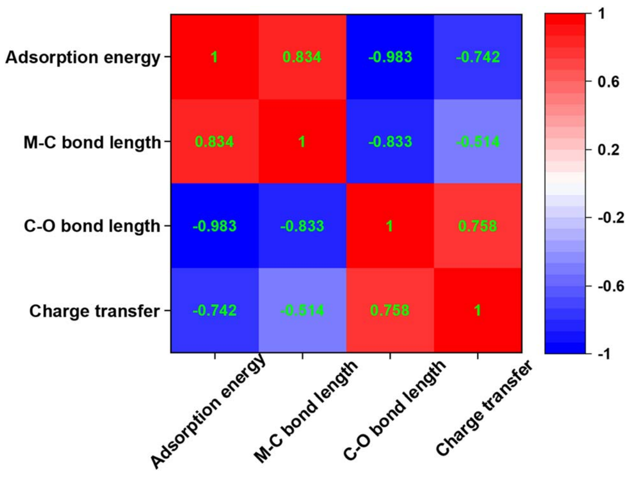

	Adsorption energy	M-C bond length	C-O bond length	Charge transfer
Adsorption energy	1	0.834	-0.983	-0.742
M-C bond length	0.834	1	-0.833	-0.514
C-O bond length	-0.983	-0.833	1	0.758
Charge transfer	-0.742	-0.514	0.758	1

Fig. 5 Pearson correlation coefficients among adsorption energy, M–C bond length, C–O bond length, and CO charge transfer.

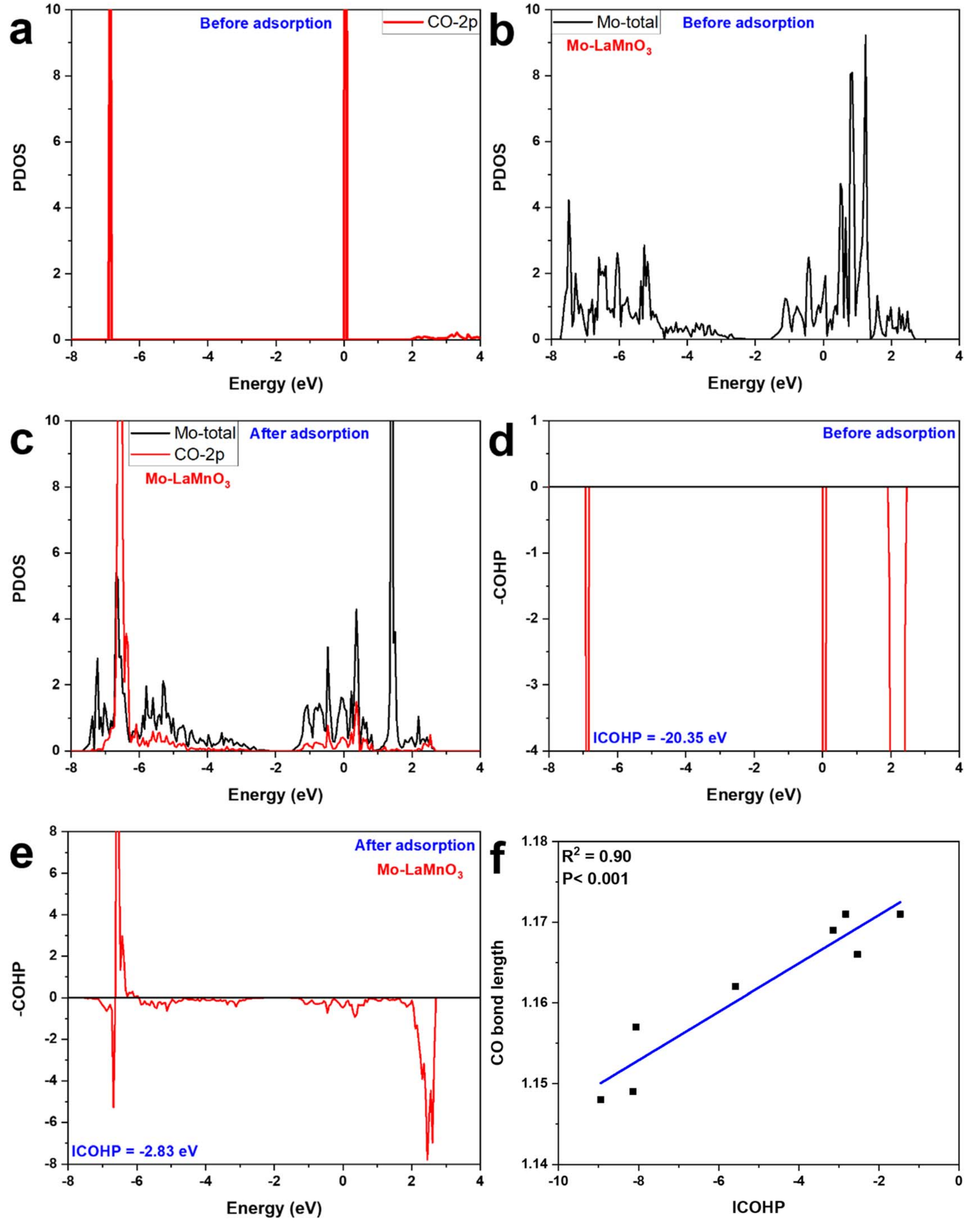

Fig. 6 (a) Partial density of states (PDOS) of the CO 2p states prior to adsorption. (b) PDOS of the total Mo states before adsorption. (c) PDOS of the total Mo and CO 2p states after adsorption. (d) Crystal orbital Hamilton population (COHP) of the C–O bond in a free CO molecule. (e) COHP of the C–O bond in the adsorbed CO molecule. (f) Linear correlation between the C–O bond integrated COHP (ICOHP) and the C–O bond length ($n = 8$).

weakening of the C–O bond. This electronic interaction is further supported by Bader charge analysis, which reveals a charge transfer of approximately 0.29 e from the surface Mo atom to the adsorbed CO molecule. The degree of CO activation can be quantitatively evaluated using the integrated crystal orbital Hamilton population (ICOHP) values. As shown in Fig. 6d and f, the ICOHP value of the C–O bond in a free CO molecule is -20.35 eV, whereas it increases to -2.83 eV upon adsorption on the Mo-LaMnO$_3$ surface, indicating a substantial weakening of the C–O bond upon adsorption. Furthermore, as illustrated in Fig. 6f, a pronounced linear correlation ($R^2 = 0.90$, $p < 0.001$) is observed between the ICOHP values of the C–O bond on different surfaces and the corresponding C–O bond lengths after adsorption. This strong correlation suggests that the C–O bond length can serve as a reliable structural descriptor for evaluating and predicting the CO activation capability of the catalysts.

3.3 Reaction mechanism of CO oxidation on doped $LaMnO_3$ surface

Fig. 7 and 8 present the reaction energy profiles and optimized geometries for CO oxidation on doped $LaMnO_3$ surfaces, respectively. The catalytic combustion of CO on these catalysts proceeds *via* two elementary steps: CO_2 formation and CO_2 desorption. For all catalysts, two distinct reaction pathways are identified for CO oxidation, involving reactions with lattice oxygen O_1 and lattice oxygen O_2. These two pathways are denoted by black and red lines in Fig. 7, respectively. During the calculations, the adsorption configuration of CO_2 was chosen as the most stable structure located near the oxygen vacancy. As shown in Fig. 8, except for Ni-$LaMnO_3$ and Cd-$LaMnO_3$, the generated CO_2 molecule is adsorbed in a nearly parallel configuration above the oxygen vacancy, forming M–O and Mn–O bonds, where M denotes the dopant atom. On the Ni-$LaMnO_3$ surface, the CO_2 molecule preferentially adsorbs above the Ni atom, whereas on the Cd-$LaMnO_3$ surface, CO_2 adopts a vertical adsorption configuration above the oxygen vacancy.

Overall, on all investigated catalyst surfaces, the reaction pathway involving lattice O_1 exhibits a lower rate-determining energy barrier than that involving lattice O_2, indicating that lattice O_1 is intrinsically more reactive. For Ti-$LaMnO_3$ and V-$LaMnO_3$, the rate-determining step is identified as CO_2 desorption, with corresponding energy barriers of 2.071 eV and 1.828 eV, respectively. In contrast, for Cr-$LaMnO_3$, pristine $LaMnO_3$, Ni-$LaMnO_3$, Mo-$LaMnO_3$, Rh-$LaMnO_3$, and Cd-$LaMnO_3$ surfaces, the formation of CO_2 constitutes the rate-determining step, with energy barriers of 1.909 eV, 1.990 eV, 0.770 eV, 2.370 eV, 1.183 eV, and 0.831 eV, respectively. Notably, the reaction energy barriers on V-$LaMnO_3$, Cr-$LaMnO_3$, Ni-$LaMnO_3$, Rh-$LaMnO_3$, and Cd-$LaMnO_3$ are lower than that on pristine $LaMnO_3$, highlighting the effectiveness of the doping strategy in enhancing catalytic activity. Among all catalysts, Ni-$LaMnO_3$ exhibits the lowest reaction energy barrier, which is reduced by 61% compared with pristine $LaMnO_3$. The reasons behind the higher activity of the O_1 site relative to O_2, as well as the pronounced energy-barrier reduction observed for Ni-$LaMnO_3$, are discussed in Section 3.5, where a detailed electronic-level analysis and mechanistic explanation are provided.

3.4 Kinetic stability analysis

To further evaluate the kinetic stability of the screened doped systems—namely V-$LaMnO_3$, Cr-$LaMnO_3$, Ni-$LaMnO_3$, Rh-$LaMnO_3$, and Cd-$LaMnO_3$—which exhibit lower CO oxidation energy barriers than pristine $LaMnO_3$, AIMD simulations were performed over a temperature range of 800–1200 K with an interval of 100 K, with pristine $LaMnO_3$ included as a reference system. The final configurations obtained from the AIMD simulations are presented in Fig. S4. It should be noted that once a structure was found to become unstable at a certain temperature, AIMD simulations at higher temperatures were not further conducted for that system. This approach enables a reliable assessment of kinetic stability while maintaining computational efficiency. The maximum temperatures at which V-$LaMnO_3$, Cr-$LaMnO_3$, pristine $LaMnO_3$, Ni-$LaMnO_3$, Rh-$LaMnO_3$, and Cd-$LaMnO_3$ remained structurally stable were 800 K, 1000 K, 1200 K, 900 K, 900 K, and 800 K, respectively. At these temperatures, the dopant atoms remained firmly anchored at their designated substitutional sites, and no significant structural distortion or framework collapse was observed.

In addition to the structural snapshots, the bond length fluctuations of the key M–O_1 bonds during the AIMD trajectories were further analysed to quantitatively assess the kinetic stability of the systems. As shown in Fig. S5, the M–O_1 bond lengths exhibit only minor thermal fluctuations without any abrupt bond breaking or significant elongation, indicating that the local bonding environments are well preserved throughout the simulations. This further indicates the doped structures integrity under elevated temperatures and confirms their kinetic stability.

Overall, these results demonstrate that the selected doped catalysts exhibit good kinetic stability at temperatures above 800 K, which are representative of practical CLC operating conditions, thereby confirming their suitability for stable CLC operation.

3.5 Structure–activity–stability relationships of doped $LaMnO_3$

To establish quantitative relationships between the intrinsic properties of doped $LaMnO_3$ and their catalytic performance in CO oxidation, it is essential to identify reliable descriptors that can simultaneously capture stability and activity. In heterogeneous catalysis, such descriptors are essential for rational catalyst screening and mechanistic understanding, as they establish a direct link between electronic structural features and catalytic performance. Accordingly, in this section, a series of electronic descriptors are systematically examined to elucidate how transition-metal doping modulates the thermodynamic stability and CO oxidation activity of $LaMnO_3$-based oxygen carriers.

Based on this framework, we first explored the correlations between formation energy (E_f) and several representative descriptors, including the electronegativity of the doped single atom (χ), the first ionization energy of the doped atom (IE), the atomic radius of the doped atom (r_{atom}), and the +3 ionic radius of the dopant atom (${r_{ion}}^{3+}$), as shown in Fig. 9. The corresponding numerical values of these descriptors are summarized in Table S2. Among them, the χ shows a moderate correlation with E_f ($R^2 = 0.41$, $p < 0.01$), following a parabolic dependence, suggesting the existence of an optimal electronegativity range that stabilizes the doped system. A similar parabolic relationship is observed for IE, which yields a slightly weaker correlation ($R^2 = 0.33$, $p < 0.05$), indicating that both excessively low and high ionization energies are unfavourable for thermodynamic stability. In contrast, the r_{atom} exhibits a weak correlation with E_f ($R^2 = 0.10$, $p > 0.1$), displaying an approximately linear

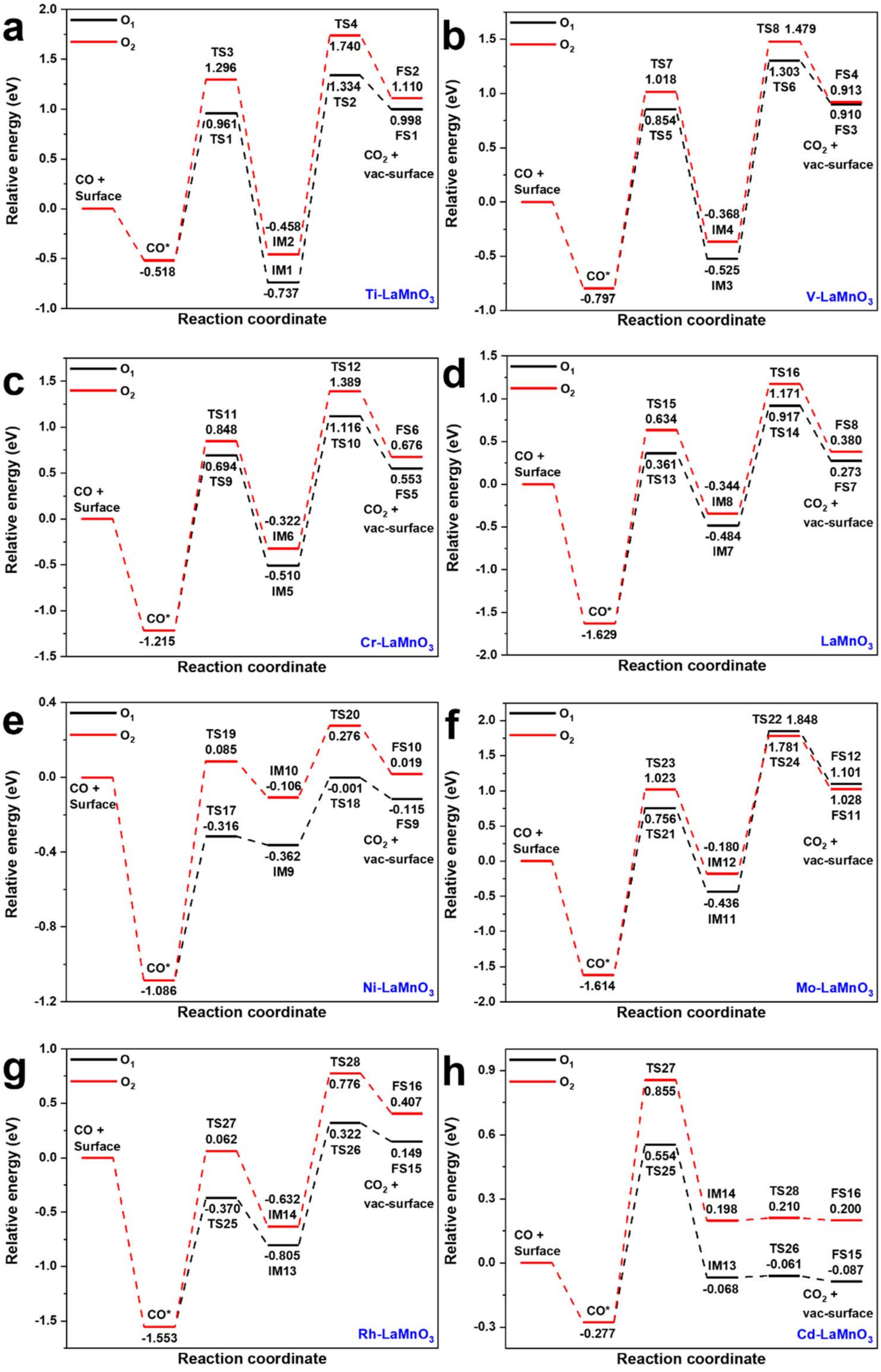

Fig. 7 Reaction energy profiles for CO oxidation on (a) Ti-LaMnO$_3$, (b) V-LaMnO$_3$, (c) Cr-LaMnO$_3$, (d) pristine LaMnO$_3$, (e) Ni-LaMnO$_3$, (f) Mo-LaMnO$_3$, (g) Rh-LaMnO$_3$, and (h) Cd-LaMnO$_3$ surfaces.

trend with limited statistical significance. This suggests that the size of the neutral dopant atom alone is insufficient to capture the key factors governing the formation energy. Notably, the $r_{\text{ion}}{}^{3+}$ demonstrates the strongest correlation with E_f ($R^2 = 0.78$, $p < 0.001$), also following a pronounced parabolic trend. This strong dependence highlights the critical role of ionic size matching between the dopant and the host lattice, reflecting the importance of lattice distortion and local structural accommodation in determining the thermodynamic stability of the doped systems.

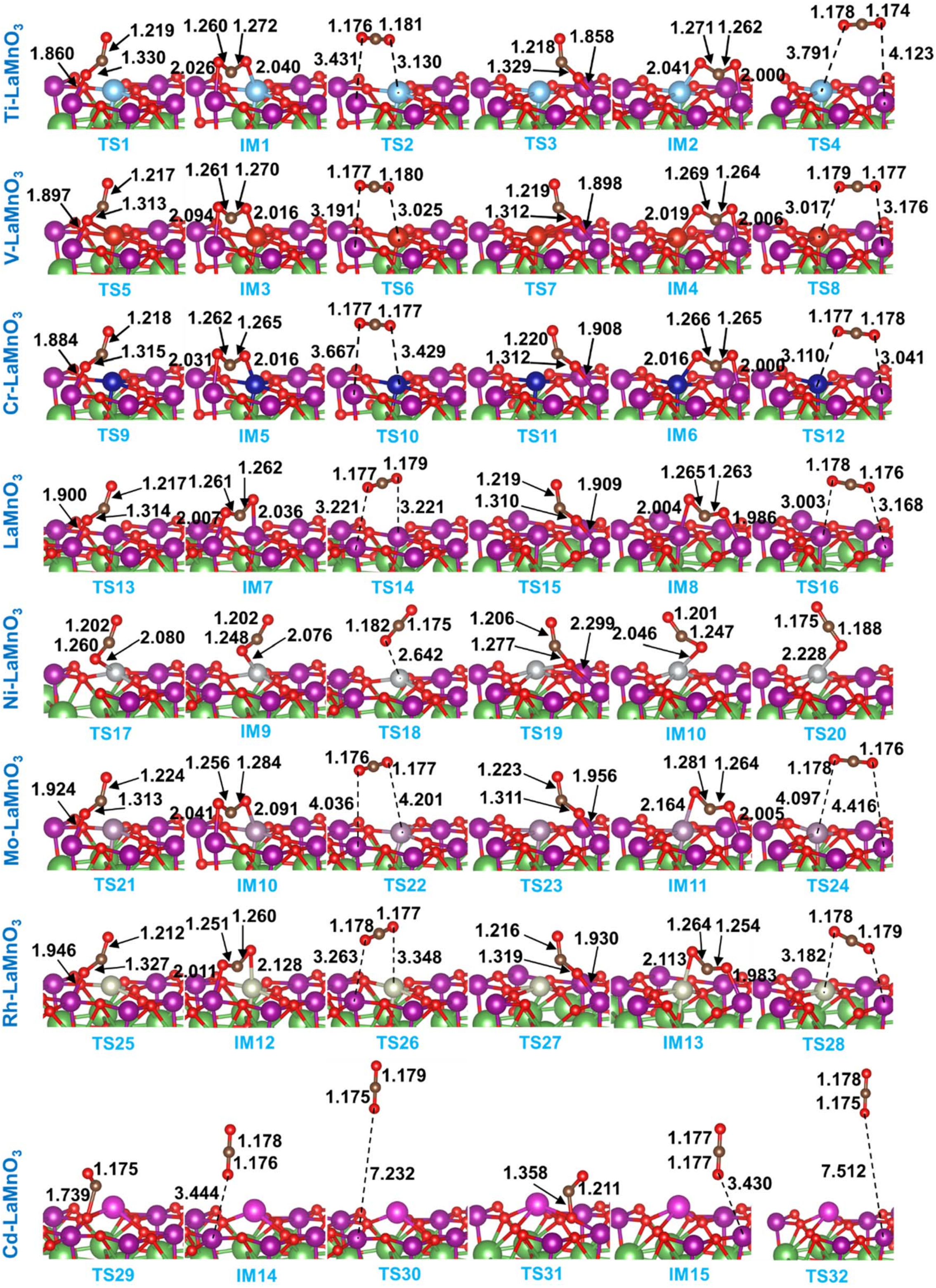

Fig. 8 Optimized geometries of CO catalytic combustion on the corresponding catalysts. The unit for bond length is Å. Atom colours: Mn (purple), La (green), O (red), and C (brown).

Based on the above analysis, the $r_{\mathrm{ion}}{}^{3+}$ emerges as the most effective descriptor for predicting the E_f among the examined physicochemical parameters with the relation equation of $y = 0.00459x^2 - 0.56676x + 17.4296$, highlighting the dominant role of ionic size effects in dopant stabilization. Specifically, stable doping requires that the dopant atom can adopt a stable +3

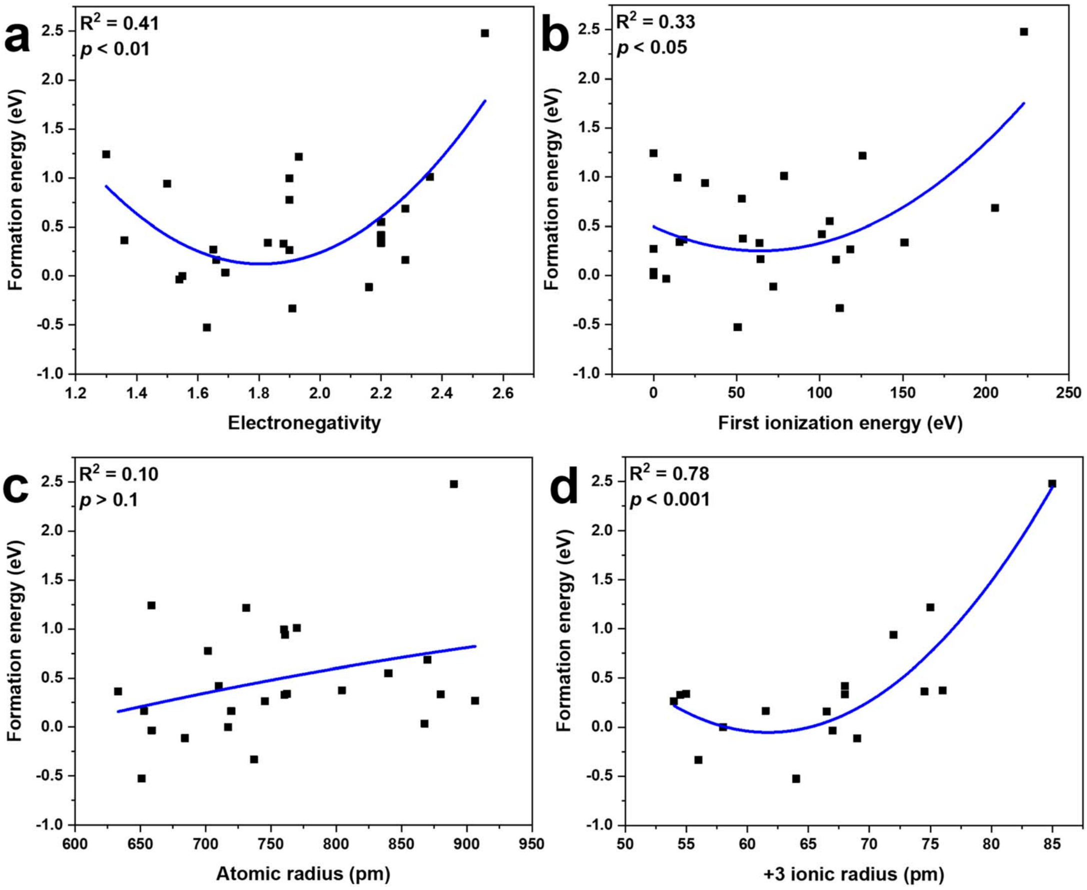

Fig. 9 Correlations between the formation energy (E_f) and (a) electronegativity of the doped single atom (χ), (b) the first ionization energy of the doped atom (IE), (c) the atomic radius of the doped atom (r_{atom}), and (d) the +3 ionic radius of the dopant atom ($r_{ion}{}^{3+}$).

oxidation state at the substitutional site, consistent with the local charge balance and coordination environment of the host lattice. In addition, the ionic radius of the dopant should be close to that of the host Mn^{3+} ion (58 pm). In this study, the dopants that lead to stable configurations exhibit +3 ionic radii ranging from 54 to 69 pm. When the dopant ionic radius is too small, the local coordination environment becomes under-coordinated, generating lattice strain and destabilizing the structure. Conversely, when the ionic radius is too large, the dopant causes excessive lattice distortion and steric repulsion, also increasing the formation energy. These observations are consistent with the classical Goldschmidt tolerance factor framework, as well as with previous studies on doped perovskites and other oxide materials.[54,55] In addition, recent studies have highlighted that ionic radius serves as a key geometric descriptor governing perovskite stability, formability, and physicochemical properties.[56,57] These results indicate that both the oxidation state and the size compatibility of the dopant are key factors in determining the thermodynamic stability of doped $LaMnO_3$, making the $r_{ion}{}^{3+}$ a physically meaningful and predictive descriptor.

In addition, we examined the correlations between the reaction energy barrier and a set of electronic descriptors, namely the d-band centre of the doped atom (ε_d), the p-band center of the O_1 atom (ε_p), the charge-transfer energy (defined as the energy difference between the orbital centers of the occupied O_1-p states and the unoccupied metal-d states, Δ), and the Bader charge transfer of the doped atom (Δq), as illustrated in Fig. 10. The corresponding numerical values of these electronic descriptors are summarized in Table S3. The O_1 site was chosen for detailed investigation due to its higher intrinsic reactivity compared to the O_2 site, which is reflected in the lower calculated reaction energy barriers. All examined electronic descriptors exhibit approximately linear correlations with the reaction energy barriers, although their predictive strengths vary considerably. The d-band centre of the dopant atom shows a weak correlation with the barrier ($R^2 = 0.26$, $p > 0.1$), indicating that variations in the dopant d-orbital energies alone are insufficient to reliably predict reaction energetics. In contrast, the p-band centre of the O_1 atom demonstrates a moderate correlation ($R^2 = 0.67$, $p < 0.05$), suggesting that the electronic structure of the lattice oxygen partially reflects the activation of the O_1 site. The Δ, defined as the energy difference between the orbital centres of the occupied O-p states and the unoccupied metal-d states, shows a stronger correlation ($R^2 = 0.73$, $p < 0.01$), highlighting the importance of dopant–lattice electron interactions in modulating the reaction barrier. Among all descriptors, the Δq exhibits the strongest predictive performance, with

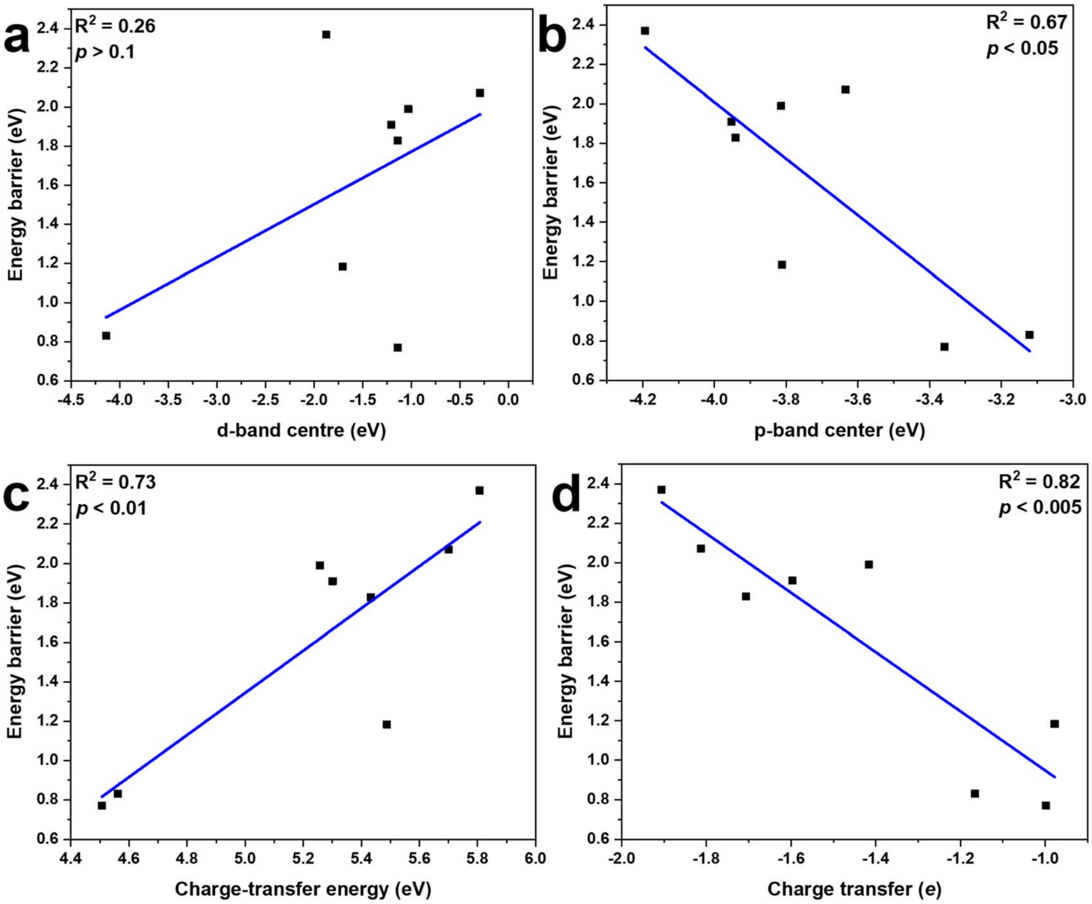

Fig. 10 Correlations between the reaction energy barrier and (a) d-band centre of the doped atom (ε_d), (b) the p-band center of the O_1 atom (ε_p), (c) the charge-transfer energy (Δ), and (d) the Bader charge transfer of the doped atom (Δq).

$R^2 = 0.82$ ($p < 0.005$), and the relationship can be described by the linear equation $y = -1.49972x - 0.55196$. Here, negative values of the Δq indicate that the dopant atom loses electrons during the doping process.

The observed trend, in which smaller Δq corresponds to lower reaction energy barriers, can be rationalized in terms of the M–O_1 bond strength. When the dopant atom loses fewer electrons to the lattice (*i.e.*, lower charge transfer), the M–O_1 bond is moderately weakened compared to the undoped lattice. This moderate weakening facilitates the activation of the O_1 site, lowering the energy barrier for bond cleavage or reaction with adsorbates. Conversely, excessive electron transfer from the dopant over-stabilizes the M–O_1 bond, increasing its bond strength and making the O_1 site less reactive, which raises the reaction barrier. To further validate this explanation, we examined the relationship between the M–O_1 bond strength, quantified by the ICOHP, and the reaction energy barrier. Higher ICOHP values correspond to weaker M–O_1 bonds. As shown in Fig. S6, a strong negative correlation is observed ($R^2 = 0.85$, $p < 0.001$), indicating that larger ICOHP values are associated with lower reaction energy barriers, which indirectly supports the mechanistic rationale described above. Therefore, the Bader charge transfer serves as a physically meaningful descriptor, as it directly reflects the electronic modulation of the M–O_1 bond, which governs the reactivity of the lattice oxygen and the corresponding reaction energetics.

Based on this analysis, the proposed mechanistic framework explains why Ni-$LaMnO_3$ exhibits the best performance, achieving a 61% reduction in the reaction energy barrier compared with pristine $LaMnO_3$. Specifically, Ni doping results in the lowest charge transfer, leading to the weakest M–O_1 bond, as evidenced by the ICOHP values in Fig. S5. This weakened bonding facilitates lattice oxygen activation, allowing CO to more readily react with the O_1 site to form CO_2, thereby enhancing catalytic activity. Furthermore, the higher activity of the O_1 site relative to O_2 can be attributed to their distinct structural environments: the O_1 atom is slightly protruded from the surface, whereas the O_2 atom is located slightly below it. Consequently, the La–O_1 distance is longer than the La–O_2 distance, indicating a weaker La–O_1 interaction. This is further supported by the ICOHP analysis (Table S4), where the La–O_1 bonds consistently exhibit higher ICOHP values than La–O_2, reflecting weaker bonding interactions. As a result, the O_1 atom is less strongly bound within the lattice and can more readily participate in oxidation reactions, accounting for its higher catalytic activity.

3.6 Discussion

In the present work, like other studies in the literature, the AIMD simulations are limited to the picosecond timescale, and long-term phenomena such as dopant migration or lattice oxygen depletion under extended CLC cycling are not captured. Nevertheless, such simulations provide effective screening of kinetically stable structures, and future studies employing machine learning potentials enable long-time simulations or experiments may be able to evaluate their durability under practical operating conditions.[58]

In addition to the timescale limitation, it should be noted that $LaMnO_3$ is a strongly correlated magnetic oxide, and that spin polarization can play an important role in accurately describing its electronic structure. In the present study, spin polarization was not explicitly considered, as the focus is placed on comparing relative trends among different doped systems using a consistent computational framework. Nevertheless, the obtained results are in qualitative agreement with experimental observations.[59] Therefore, the main conclusions of this work are expected to remain valid in terms of the trends revealed. To further assess the influence of spin polarization, a comparison of adsorption sites, structural parameters (d(M–C) and d(C–O), Å), Bader charge transfer (Q, e), and adsorption energies (E_{ads}, eV) was performed for CO adsorption on Ti-, V-, Cr-, Ni-, Mo-, Rh-, and Cd-doped $LaMnO_3$ surfaces using non-spin-polarized (NSP) and spin-polarized (SP) calculations (Table S5). The results indicate that the preferred adsorption sites remain unchanged, while only minor variations in structural parameters are observed (typically within $\sim$0.1 Å). However, more pronounced differences are observed in adsorption energies for certain dopants. In particular, Ti- and Ni-doped systems exhibit significantly weaker adsorption in SP calculations compared to NSP results, as reflected by adsorption energies shifting toward less negative values by approximately 55% and 40%, respectively. This indicates that spin polarization can have a substantial quantitative impact on adsorption energetics in these cases. Similar but less pronounced reductions are also observed for Cr and Rh. In contrast, V and Mo exhibit slightly enhanced adsorption under SP conditions, with Mo showing the most notable increase, while Cd-doped systems display minimal sensitivity to spin polarization. These distinct behaviours originate from the dopant-dependent electronic configurations, where partially filled d orbitals (d-electron states) in Ti and Ni lead to pronounced spin-induced redistribution near the Fermi level, while the closed-shell d^{10} configuration of Cd results in negligible spin sensitivity. Other dopants exhibit intermediate behaviour, reflecting a balance between these two limiting electronic configurations. Notably, the changes in adsorption energies are accompanied by variations in charge transfer and slight modifications of the C–O bond length, further supporting a spin-dependent interaction mechanism. Overall, although spin polarization affects the quantitative values of adsorption properties, it does not alter the relative trends among different dopants, and thus the main conclusions of this work remain qualitatively reliable.

Furthermore, the present study employs a single dopant substitution model to investigate the intrinsic effects of different dopant species on the electronic structure and catalytic performance of $LaMnO_3$. This approach enables a clear comparison of dopant-dependent trends by minimizing dopant–dopant interactions. In practical systems, higher dopant concentrations may introduce additional effects such as dopant–dopant coupling, clustering, or phase segregation, which may further influence catalytic behaviour. These aspects may be considered in future studies. The current results therefore provide fundamental insights into the role of individual dopants and can serve as a useful basis for follow-on investigations.

In addition to the catalytic activity trends, the practical feasibility of the dopants should also be considered for real CLC applications. Some dopants investigated in this work, such as Rh and Cd, may have issues with high cost and potential toxicity, which could limit their large-scale implementation. Nevertheless, these dopants are included here to provide a comprehensive understanding of the intrinsic electronic and catalytic effects induced by different dopant species, thereby establishing a general mechanistic framework. In practical systems, a balance between catalytic performance, cost, and environmental impact is essential. Transition metal dopants such as Ni and Cr, which are more abundant and cost-effective, may therefore be more promising candidates for practical CLC applications. To provide a quantitative comparison, the reaction energy barriers for CO conversion on Cr-, Ni-, Cd-, and Rh-doped $LaMnO_3$ systems are calculated to be 1.909 eV, 0.770 eV, 0.831 eV, and 1.183 eV, respectively. These results indicate that Ni and Cd dopants significantly reduce the reaction barrier compared to Cr and Rh, with Ni exhibiting the lowest barrier among all investigated systems. Furthermore, AIMD simulations were performed to evaluate the thermal stability of the corresponding doped $LaMnO_3$ systems. The results show that the Cr-, Ni-, Cd-, and Rh-doped systems remain structurally stable up to approximately 1000 K, 900 K, 800 K, and 900 K, respectively. This suggests that although Cr-$LaMnO_3$ exhibits the highest thermal stability, Ni-$LaMnO_3$ provides the most favourable balance between catalytic activity and structural stability among the studied dopants. The insights obtained in this study can serve as useful guidelines for the rational selection and design of dopants with both high activity and improved feasibility.

4 Conclusions

In summary, we employed DFT calculations to investigate the effects of B-site single-atom doping on $LaMnO_3$ for CO chemical looping combustion. First, the stability of the doped materials was evaluated, and among 25 possible configurations, eight thermodynamically stable structures were identified. Next, the adsorption and activation of CO on these doped surfaces were examined, with detailed insights provided at the electronic level. Subsequently, the CO oxidation mechanisms and reaction energy barriers were analysed, revealing five doped structures (V-, Cr-, Ni-, Rh-, and Cd-$LaMnO_3$) exhibiting lower reaction barriers than pristine $LaMnO_3$, with Ni-$LaMnO_3$ showing the lowest barrier of 0.770 eV, representing a 61% reduction compared to the undoped material. The dynamical stability of these low-barrier structures was further confirmed *via* AIMD simulations at CLC temperatures, demonstrating their kinetic stability under reaction conditions. Finally, the structure–activity–stability relationships of the doped $LaMnO_3$ were established, highlighting that the +3 ionic radius and the Bader charge transfer of the doped atom serve as robust descriptors for predicting both the thermodynamic stability and catalytic activity of the doped catalysts.

Conflicts of interest

There are no conflicts to declare.

Data availability

The authors confirm that the data supporting the findings of this study are available within the article and its supplementary information (SI). Supplementary information is available. See DOI: https://doi.org/10.1039/d6ta01727d.

Acknowledgements

The research is supported by Carbon Neutrality and Energy System Transformation (CNEST) Program led by Tsinghua University. Support from the UK Engineering and Physical Sciences Research Council under the project "UK Consortium on Mesoscale Engineering Sciences (UKCOMES)" (Grant No. EP/X035875/1) is also acknowledged. This work made use of computational support by CoSeC, the Computational Science Centre for Research Communities, through UKCOMES.

References

1 N. Shehzad, M. Tahir, K. Johari, T. Murugesan and M. Hussain, A critical review on TiO2 based photocatalytic CO2 reduction system: Strategies to improve efficiency, *J. CO_2 Util.*, 2018, **26**, 98–122.

2 W. Gao, S. Liang, R. Wang, Q. Jiang, Y. Zhang, Q. Zheng, *et al.*, Industrial carbon dioxide capture and utilization: state of the art and future challenges, *Chem. Soc. Rev.*, 2020, **49**(23), 8584–8686.

3 J. Wang, X. Z. Jiang and K. H. Luo, Exploring reaction mechanism for ammonia/methane combustion via reactive molecular dynamics simulations, *Fuel*, 2023, **331**, 125806.

4 B. Metz, O. Davidson, H. De Coninck, M. Loos and L. Meyer, *IPCC Special Report on Carbon Dioxide Capture and Storage*, Cambridge University Press, Cambridge, 2005.

5 M. Ishida, D. Zheng and T. Akehata, Evaluation of a chemical-looping-combustion power-generation system by graphic exergy analysis, *Energy*, 1987, **12**(2), 147–154.

6 M. Anheden and G. Svedberg, Exergy analysis of chemical-looping combustion systems, *Energy Convers. Manage.*, 1998, **39**(16–18), 1967–1980.

7 A. Lyngfelt, B. Leckner and T. Mattisson, A fluidized-bed combustion process with inherent CO2 separation; application of chemical-looping combustion, *Chem. Eng. Sci.*, 2001, **56**(10), 3101–3113.

8 A. Abdalla, M. Mohamedali and N. Mahinpey, Recent progress in the development of synthetic oxygen carriers for chemical looping combustion applications, *Catal. Today*, 2023, **407**, 21–51.

9 M. Qasim, M. Ayoub, N. A. Ghazali, A. Aqsha and M. Ameen, Recent advances and development of various oxygen carriers for the chemical looping combustion process: a review, *Ind. Eng. Chem. Res.*, 2021, **60**(24), 8621–8641.

10 F. Liu, R. Fang, X. Wang, J. Liu and Y. Li, The reaction characteristics and mechanism of pine sawdust chemical-looping gasification based on CoFe2O4 oxygen carrier, *Renewable Energy*, 2022, **195**, 1300–1309.

11 X. Zhu, K. Li, L. Neal and F. Li, Perovskites as geo-inspired oxygen storage materials for chemical looping and three-way catalysis: a perspective, *ACS Catal.*, 2018, **8**(9), 8213–8236.

12 Z. Sarshar, F. Kleitz and S. Kaliaguine, Novel oxygen carriers for chemical looping combustion: La 1− x Ce x BO 3 (B= Co, Mn) perovskites synthesized by reactive grinding and nanocasting, *Energy Environ. Sci.*, 2011, **4**(10), 4258–4269.

13 Z. Sarshar, Z. Sun, D. Zhao and S. Kaliaguine, Development of sinter-resistant core–shell LaMn x Fe1−x O3@ mSiO2 oxygen carriers for chemical looping combustion, *Energy Fuels*, 2012, **26**(5), 3091–3102.

14 Z. Bai and K. H. Luo, A density functional theory study of CH4 oxidation over LaMnO3 oxygen carrier during chemical looping combustion, *Fuel Process. Technol.*, 2026, **284**, 108418.

15 X. Ma, J. Liu and Y. Yang, Experimental and theoretical studies on the reactivity and reaction mechanism of LaMnO3 with CO in chemical looping combustion, *J. Energy Inst.*, 2024, **112**, 101462.

16 Z. Bai and K. H. Luo, Mechanistic study of Hg0 oxidation over LaMnO3 oxygen carrier during chemical looping combustion, *Chem. Eng. J.*, 2025, 166154.

17 Z. Bai and K. H. Luo, Mechanisms for interactions of H2S and Hg0 with oxygen carrier LaMnO3 during chemical looping combustion: a DFT study, *Carbon Capture Sci. Technol.*, 2025, 100480.

18 E. R. Monazam, R. Siriwardane, R. W. Breault, H. Tian, L. J. Shadle, G. Richards, *et al.*, Kinetics of the reduction of CuO/bentonite by methane (CH4) during chemical looping combustion, *Energy Fuels*, 2012, **26**(5), 2779–2785.

19 C. Zheng, M. Su and H. Zhao, Microkinetic analysis of reactions between CO and CuO in chemical looping combustion, *Combust. Flame*, 2025, **273**, 113967.

20 P. H. T. Ngamou, K. Kohse-Höinghaus and N. Bahlawane, CO and ethanol oxidation over LaCoO3 planar model catalysts: Effect of the thickness, *Catal. Commun.*, 2011, **12**(14), 1344–1350.

21 D. Guan, H. Xu, Q. Zhang, Y. C. Huang, C. Shi, Y. C. Chang, *et al.*, Identifying a universal activity descriptor and a unifying mechanism concept on perovskite oxides for

green hydrogen production, *Adv. Mater.*, 2023, **35**(44), 2305074.

22 D. Xu, W. Qu, X. Gu, M. Li, R. Liu, Y. Dong, *et al.*, An activity descriptor for perovskite oxides in catalysis, *Chem Catal.*, 2022, **2**(5), 1163–1176.

23 R. Jacobs, J. Liu, H. Abernathy and D. Morgan, Critical assessment of electronic structure descriptors for predicting perovskite catalytic properties, *ACS Appl. Energy Mater.*, 2024, **7**(8), 3366–3377.

24 W.-J. Yin, Density functional theory-free descriptor for the practical discovery of perovskite catalysts, *Comput. Mater. Sci.*, 2021, **193**, 110342.

25 S. Zhang, L. Tao, T. Fang, J. Dang, D. Dastan, L. Li, *et al.*, Resolving Competitive Adsorption Pathways on Ir-WSe2 Nanosheets via DFT Simulations for Ultra-Selective NO Recognition in Harsh Environments, *ACS Appl. Nano Mater.*, 2026, 4367–4377.

26 M. Lu, L. Tao, Y. Su, Y. Sun, D. Dastan, J. Rehman, *et al.*, First-Principles Study of Bonding-Driven Selectivity in CO2 Electroreduction on Metal–Nitrogen–Carbon Catalysts, *J. Phys. Chem. C*, 2025, 326–335.

27 S. Nie, L. Tao, H. Yu, D. Dastan, W. Wang, L. Hong, *et al.*, Theoretical and machine learning exploration of electronic factors governing Ni-centered CO 2 reduction catalysts, *Phys. Chem. Chem. Phys.*, 2025, **27**(40), 21810–21823.

28 Y. Sun, L. Tao, Y. Su, D. Dastan, H. Zhang, H. Zhao, *et al.*, Emerging two-dimensional supported atomic and cluster catalysts for CO2 electroreduction, *Nanoscale Horiz.*, 2026, 1239–1279.

29 Y. Sun, L. Tao, M. Wu, D. Dastan, J. Rehman, L. Li, *et al.*, Multi-atomic loaded C 2 N 1 catalysts for CO 2 reduction to CO or formic acid, *Nanoscale*, 2024, **16**(20), 9791–9801.

30 U. G. Singh, J. Li, J. W. Bennett, A. M. Rappe, R. Seshadri and S. L. Scott, A Pd-doped perovskite catalyst, BaCe1− xPdxO3−δ, for CO oxidation, *J. Catal.*, 2007, **249**(2), 349–358.

31 Y. Farhang, E. Taheri-Nassaj and M. Rezaei, Pd doped LaSrCuO4 perovskite nano-catalysts synthesized by a novel solid state method for CO oxidation and Methane combustion, *Ceram. Int.*, 2018, **44**(17), 21499–21506.

32 Y. Farhang, E. Taheri-Nassaj and M. Rezaei, Enhanced methane combustion and CO oxidation with Pd and Pt substitution LaSrCuO4 perovskites, *Mater. Today Commun.*, 2023, **36**, 106891.

33 X. Yuan, L. Meng, C. Zheng and H. Zhao, Deep insight into the mechanism of catalytic combustion of CO and CH4 over SrTi1−x B x O3 (B= Co, Fe, Mn, Ni, and Cu) perovskite via flame spray pyrolysis, *ACS Appl. Mater. Interfaces*, 2021, **13**(44), 52571–52587.

34 Y. Yang, X. Yan, J. Liu, F. Liu and Y. Li, Reaction mechanism and microkinetics of CO catalytic combustion over Ni-doped LaCoO3 perovskite, *Proc. Combust. Inst.*, 2023, **39**(4), 5621–5635.

35 Z. Bai, X. Z. Jiang and K. H. Luo, Enhanced CO2 electrochemical reduction on single-atom catalysts with optimized environmental, central and axial chemical ambient, *J. Colloid Interface Sci.*, 2025, **686**, 1188–1199.

36 Z. Bai, X. Z. Jiang and K. H. Luo, Effects of Electric Field on Chemical Looping Combustion: A DFT Study of CO Oxidation on CuO (111) Surface, *ACS Omega*, 2024, **9**(19), 21082–21088.

37 Z. Bai, Z. Zhi, X. Z. Jiang and K. H. Luo, Rational Design of Dual-Atom Catalysts for Electrochemical CO2 Reduction to C1 and C2 Products with High Activity and Selectivity: A Density Functional Theory Study, *Ind. Eng. Chem. Res.*, 2025, **64**(8), 4378–4387.

38 Z. Bai, X. Z. Jiang and K. H. Luo, Theoretical exploration on the performance of single and dual-atom Cu catalysts on the CO 2 electroreduction process: a DFT study, *Phys. Chem. Chem. Phys.*, 2023, **25**(35), 23717–23727.

39 A. Jain, S. P. Ong, G. Hautier, W. Chen, W. D. Richards, S. Dacek, *et al.*, Commentary: The Materials Project: A materials genome approach to accelerating materials innovation, *APL Mater.*, 2013, **1**(1), 011002.

40 A. L. Gavin and G. W. Watson, Modelling oxygen defects in orthorhombic LaMnO 3 and its low index surfaces, *Phys. Chem. Chem. Phys.*, 2017, **19**(36), 24636–24646.

41 Z. Wang, J. Liu, Y. Yang, Y. Yu, X. Yan and Z. Zhang, Insights into the catalytic behavior of LaMnO3 perovskite for Hg0 oxidation by HCl, *J. Hazard. Mater.*, 2020, **383**, 121156.

42 G. Kresse and J. Furthmüller, Efficiency of ab-initio total energy calculations for metals and semiconductors using a plane-wave basis set, *Comput. Mater. Sci.*, 1996, **6**(1), 15–50.

43 G. Kresse and J. Hafner, Ab initio molecular dynamics for liquid metals, *Phys. Rev. B:Condens. Matter Mater. Phys.*, 1993, **47**(1), 558.

44 J. P. Perdew, K. Burke and M. Ernzerhof, Generalized gradient approximation made simple, *Phys. Rev. Lett.*, 1996, **77**(18), 3865.

45 G. Henkelman, B. P. Uberuaga and H. Jónsson, A climbing image nudged elastic band method for finding saddle points and minimum energy paths, *J. Chem. Phys.*, 2000, **113**(22), 9901–9904.

46 V. Wang, N. Xu, J.-C. Liu, G. Tang and W.-T. Geng, VASPKIT: A user-friendly interface facilitating high-throughput computing and analysis using VASP code, *Comput. Phys. Commun.*, 2021, **267**, 108033.

47 W. Yi, G. Tang, X. Chen, B. Yang and X. Liu, qvasp: A flexible toolkit for VASP users in materials simulations, *Comput. Phys. Commun.*, 2020, **257**, 107535.

48 K. Momma and F. Izumi, VESTA: a three-dimensional visualization system for electronic and structural analysis, *Appl. Crystallogr.*, 2008, **41**(3), 653–658.

49 S. Maintz, V. L. Deringer, A. L. Tchougréeff and R. Dronskowski., *LOBSTER: a Tool to Extract Chemical Bonding from Plane-wave Based DFT*, Wiley Online Library, 2016.

50 S. Faridi, S. Razzaq, D. Singh, L. Meng, F. Viñes, F. Illas, *et al.*, Trends in competing oxygen and chlorine evolution reactions over electrochemically formed single-atom centers of MXenes, *J. Mater. Chem. A*, 2025, **13**(22), 16481–16490.

51 M. Pishahang, C. Mohn, S. Stølen and E. Bakken, DFT-study of the energetics of perovskite-type oxides LaMO3 (M= Sc–Cu), *RSC Adv.*, 2012, **2**(28), 10667–10672.

52 C. Jiang, H. Song, G. Sun, X. Chang, S. Zhen, S. Wu, *et al.*, Data-driven interpretable descriptors for the structure–activity relationship of surface lattice oxygen on doped vanadium oxides, *Angew. Chem., Int. Ed.*, 2022, **61**(35), e202206758.

53 J. Demaison and A. G. Császár, Equilibrium CO bond lengths, *J. Mol. Struct.*, 2012, **1023**, 7–14.

54 W. Travis, E. Glover, H. Bronstein, D. Scanlon and R. Palgrave, On the application of the tolerance factor to inorganic and hybrid halide perovskites: a revised system, *Chem. Sci.*, 2016, **7**(7), 4548–4556.

55 R. Brakkee and R. M. Williams, Minimizing defect states in lead halide perovskite solar cell materials, *Appl. Sci.*, 2020, **10**(9), 3061.

56 A. S. Gzyl, P. K. Addo and B. M. Sanchez, A new ionic radii scale derived from perovskite oxides, *J. Solid State Chem.*, 2025, **346**, 125254.

57 R. Ouyang, Exploiting ionic radii for rational design of halide perovskites, *Chem. Mater.*, 2019, **32**(1), 595–604.

58 S. Banerjee, G. Periyasamy and S. K. Pati, Possible application of 2D-boron sheets as anode material in lithium ion battery: A DFT and AIMD study, *J. Mater. Chem. A*, 2014, **2**(11), 3856–3864.

59 X. Yan, J. Liu, Y. Yang, Z. Wang and Y. Zheng, A catalytic reaction scheme for NO reduction by CO over Mn-terminated LaMnO3 perovskite: A DFT study, *Fuel Process. Technol.*, 2021, **216**, 106798.